Underlying features extraction using difference maps from manifold coordinates of hyperspectral imagery

SUN Weiwei[1], LIU Chun[1,2], SHI Beiqi[1,3], LI Weiyue[1]

1. *College of Surveying and Geo-informatics, Tongji University, Shanghai* 200092, *China*;
2. *Key Laboratory of Advanced Engineering Survey of NASMG, Shanghai* 200092, *China*;
3. *Urban Information Center, Shanghai Normal University, Shanghai* 200234, *China*

Abstract: Manifold coordinates from Isometric mapping (Isomap) and Local Tangent Space Alignment (LTSA) preserve the spectral features of ground objects from Hyperspectral Imagery (HSI) through nonlinear dimensionality reduction. However, the theoretical differences result in differing capabilities in preserving spectral features. Thus, a comparison of two coordinates can make the underlying features prominent. Therefore, this paper proposes an innovative method called Difference Maps from Manifold Coordinates (DMMC), which is based on Isomap and LTSA, to extract underlying features. First, spectral interpretations are matched with both coordinates and ensured to preserve the same spectral features. Second, the Isomap and LTSA coordinates are transformed into a uniform system using coordinate normalization and axis-direction adjustment. Finally, the difference maps are obtained through subtraction operations between the weighted manifold maps, and underlying features are extracted using classical image processing approaches. Two case studies are performed to evaluate the proposed method, and the results are compared with those obtained u sing Isomap and LTSA. The results show that DMMC outperforms Isomap and LTSA in extracting underlying features, such as the underlying shallow water near the river bank and the low spatial-resolution road in the large image scene of a swamp. This method provides a novel scheme for extracting underlying features from HSI data.

Key words: hyperspectral imagery, nonlinear dimensionality reduction, Isometric mapping, local tangent space alignment, difference maps from manifold coordinates

CLC number: TP75 **Document code:** A

Citation format: **Sun W W, Liu C, Shi B Q and Li W Y. 2013. Underlying features extraction using difference maps from manifold coordinates of hyperspectral imagery. Journal of Remote Sensing, 1 7(6): 1327 - 1443 [DOI: 10. 11834/jrs. 20132347]**

1 INTRODUCTION

In Hyperspectral Imagery (HSI), underlying features represent inconspicuous or underlying information with respect to the spectral features of ground objects. For example, HSI data have shown low-dimensional manifold features. For instance, the height difference in the bed near the river bank divides water into two regions, i. e. , the shallow and deep regions, which are characterized by the subtle differences in the characteristics of their spectrums. Likewise, in the large-scale swamp Hyperion images, a slender road is inconspicuous, and is difficult to extract due to the low spatial-resolution of Hyperion data. Underlying features usually comprise a small part of information from ground objects. Thus, such features have always been among the hottest topics in HSI data analysis. The extraction of underlying features directly benefits applications in geological explorations (Chabrillat, et al. , 2002; Wang, et al. , 2010), environment monitoring (Cheng, et al. , 2008; Pu, et al. , 2008), and ground scouting (Luo, et al. , 2010; Walsh, et al. , 2008). However, owing to the numerous bands and strong intra-band correlations, the underlying features in HSI are usually extracted after reducing dimensionality.

Manifold learning has recently been introduced into the HSI field to address the problem of underlying feature extraction. Manifold learning assumes that an HSI dataset is sampled from a low-dimension manifold and attempts to explore the underlying features by mapping the dataset into a low-dimensional manifold coordinate system. Numerous manifold learning methods are a vailable, including Isometric mapping (Isomap) (Tenenbaum, e t al. , 2000), Local Tangent Space Alignment (LTSA) (Zhang & Zha, 2003), Locally Linear Embedding (LLE) (Roweis & Saul, 2000), laplacian eigenmaps (Belkin & Niyogi, 2003) and self-o rganizing maps (Tamayo, et al. , 1999). Among these methods, Isomap and LTSA are representatives of the global and local methods, respectively (Lee & Verleysen, 2007). Isomap

Received: 2012-12-13; **Accepted:** 2013-03-05; **Version of record first published:** 2013-03-12

Foundation: National Basic Research Program of China (863 Program) (No. 2013CB733204); The 37th Scientific Research Foundation for the Returned Overseas Chinese Scholars, State Education Ministry and Key Laboratory of Advanced Engineering Surveying of State Bureau of Surveying and Mapping (No. TJES1010)

First author biography: SUN Weiwei (1985—), male, Ph. D. candidate. He majors in the theory and application of GIS-T, dimensionality reduction with hyperspectral imagery, compressive sensing, and has published 16 papers. E-mail: sw8525@ gmail. com

preserves Euclidean distances between pairwise points by embedding them with the graph distances between homologous pixels in spectral space, whereas LTSA preserves the local geometric structures of local tangent space described by the nearest neighbors of pixels. Extant literature continues to report some achievements by the two methods in extracting underlying features. For the Isomap, Bachmann introduced Isomap to exploit the manifold geometric structures for ocean studies (Bachmann, et al., 2005). Gillis a pplied manifold learning to model HSI data and found that u nderlying water scenes can be modeled as a union of one-d imensional manifold curves (Gillis, et al., 2005). Subsequently, Bachmann parameterized the nonlinear manifolds in a coastal area to represent the underlying features of the ocean scene (Bachmann, et al., 2009). Chen employed Isomap to extract more underlying features in HSI data and obtained high accuracy classification results using the shortest path k-nearest neighbor classifier (Chen, et al., 2005). Wang found underlying Isomap manifolds in training samples of HSI data, which facilitated the learning of mixed linear models for classification (Wang, et al., 2006). For the LTSA, Fong reduced the dimensionality of HSI data for the underlying LTSA manifolds and further studied classification performance (Fong, 2007). With LTSA, Ma implemented a few underlying features in an embedded space to distinguish anomalies in HSI data (Ma, et al., 2010). Subsequently, Ma i mproved LTSA and presented the Generalized Supervised Local Tangent Space Alignment (GSLTSA) method to extract nonlinear properties for classification (Ma, et al., 2010). Yang proposed the unified manifold alignment framework based on LTSA (Yang & Crawford, 2011). The framework utilizes the underlying manifold geometric features in multi-temporal HSI datasets to f acilitate classification. Crawford more recently investigated the underlying nonlinear features identified by manifold learning and proved that this method outperforms linear methods and full d imension data in terms of classification (Crawford, et al., 2011). However, existing studies extracted underlying features with a single manifold learning method and never considered exploring the underlying features using the divergences between manifold coordinates from two different methods.

With nonlinear dimensionality reduction in manifold learning, manifold coordinates represent the spectral features of ground objects. However, theoretical differences among different methods result in diverse capacities in preserving spectral features. The difference in manifold coordinates from two different methods could demonstrate the different capacities of both methods in preserving spectral features. Thus, identifying underlying features that were hidden in manifold maps through a single method became evident. The difference between two m anifold coordinates should build on the fact that the two coordinates in each dimension represent the same spectral features of ground objects. Sun proposed spectral interpretations of manifold coordinates in each dimension by comparing and observing the changing trends of manifold coordinates and spectral curves (Sun, et al., 2012). Based on spectral interpretations of manifold coordinates, this paper presents a novel method called Difference Maps of Manifold Coordinates (DMMC) for the extraction of underlying features from HSI data, thus providing a new prospect for underlying feature extraction.

2 MANIFOLD LEARNING IN HSI DATA

Manifold learning assumes that HSI data were sampled u niformly from one manifold and attempts to map the original data into low-dimensional embedded space while preserving c ertain geometric structures (Tenenbaum, et al., 2000). Isomap and LTSA respectively represent the most common global and local methods in manifold learning (Lee & Verleysen, 2007). I somap preserves the Euclidean distances between every pair of points when embedding the same with the graph distances b etween homologous pixels in spectral space (Tenenbaum, et al., 2000). LTSA can satisfactorily preserve local geometric structures (Zhang & Zha, 2003), particularly with spectral edge features in image scenes (Zhou, et al., 2009). The numerous innate differences between the two methods make them good candidates to explain the proposed method. However, our method is more suitable for use with other methods.

Let HSI data comprise a real vector set $\boldsymbol{X} = [\boldsymbol{x}_1, \cdots, \boldsymbol{x}_N]^{\mathrm{T}} \in \mathbf{R}^D$ in space $\mathbf{R}^D$, where N and D represent the number of pixels and bands, respectively, and the real vector $\boldsymbol{Y} = [\boldsymbol{y}_1, \cdots, \boldsymbol{y}_N]^{\mathrm{T}} \in \mathbf{R}^d$ denotes the manifold coordinates in an embedded space with $d << D$. Let the neighborhood for each point be $\boldsymbol{C}_i = [\boldsymbol{x}_{i_1}, \cdots, \boldsymbol{x}_{i_k}]$, where k is the neighborhood size. The methods of Isomap and LTSA in HSI are described in the following section.

2.1 Isomap method in HSI data

The Isomap method computes for the coordinates by m apping HSI data into the predefined d-dimension space. First, the neighborhood graph is constructed based on the Euclidean distance between pairwise pixels $\boldsymbol{x}_i$ and $\boldsymbol{x}_j$. If $\boldsymbol{x}_i$ and $\boldsymbol{x}_j$ lie within a neighborhood defined by a set of k-nearest neighbors, the edges between the two points are connected, with the length as the Euclidean distance; otherwise, the length is 0. Subsequently, the geodesic distance graph is constructed. For $\boldsymbol{x}_i$ and $\boldsymbol{x}_j$ within the neighborhood, the geodesic distance is the Euclidean distance. Otherwise, the geodesic distance will be replaced by the shortest path distance as determined using the Dijkstra algorithm. The largest connected components are then selected from the graph, considering the stability of the shortest path graph. Finally, multidimensional scaling is used to compute for the d-d imensional embedding. Manifold coordinates $\boldsymbol{Y}$ are the eigenvectors of the first d-largest eigenvalues of $\boldsymbol{\tau} = -\boldsymbol{HSH}/2$, where S is the squared geodesic distance matrix, and $\boldsymbol{H}$ is the concentrated matrix.

2.2 LTSA method in HSI data

The LTSA attempts to construct local geometric structures within the tangent space of each pixel, and then align the overlapping local tangent space to obtain the global manifold coordinates (Zhang & Zha, 2003). Similar to Isomap, the neighborhood graph is first constructed based on the Euclidean distance between pairwise pixels $\boldsymbol{x}_i$ and $\boldsymbol{x}_j$. Subsequently, using the d-d imensional affine subspace to approach points in each neighborhood $\boldsymbol{C}_i$, the local coordinates $\boldsymbol{\Theta}_i = \boldsymbol{Q}_i^{\mathrm{T}}(\boldsymbol{C}_i - \bar{\boldsymbol{x}}\boldsymbol{e}_k^{\mathrm{T}})$ of each pixel $\boldsymbol{x}_i$ are obtained, where $\boldsymbol{Q}_i$ represents the corresponding singular v

ectors of the largest d right singular values for the centered matrix $\boldsymbol{C}_i$, and $\bar{\boldsymbol{x}}_i = \boldsymbol{C}_i e^{\mathrm{T}}$ is the central point of $\boldsymbol{C}_i$. Finally, global coordinates $\boldsymbol{Y}$ are achieved through the affine transformation of local coordinates. Global coordinates $\boldsymbol{Y}$ are eigenvectors corresponding to 2 and to $d+1$ eigenvalues of the global alignment matrix $\boldsymbol{\Phi} = \sum_{i=1}^{N} \boldsymbol{S}_i \boldsymbol{W}_i \boldsymbol{W}_i^{\mathrm{T}} \boldsymbol{S}_i^{\mathrm{T}}$, where $\boldsymbol{S}_i = [\boldsymbol{x}_{i1}, \cdots, \boldsymbol{x}_{ik}] \in \mathbf{R}^{N \times k}$ represents the selection matrix, and $\boldsymbol{W}_i = \boldsymbol{I} - [\boldsymbol{1}_k/\sqrt{k}, \boldsymbol{V}_i][\boldsymbol{1}_k/\sqrt{k}, \boldsymbol{V}_i]^{\mathrm{T}}$ for the corresponding singular vectors $\boldsymbol{V}_i$ of the largest d left singular values in each centered matrix $\boldsymbol{C}_i$.

3 EXTRACTING UNDERLYING FEATURES USING THE DMMC METHOD

The DMMC method extracts underlying features by using the divergence between two manifold coordinates to preserve the spectral features of ground objects. As shown in Fig. 1, the DMMC method with Isomap and LTSA includes the following steps:

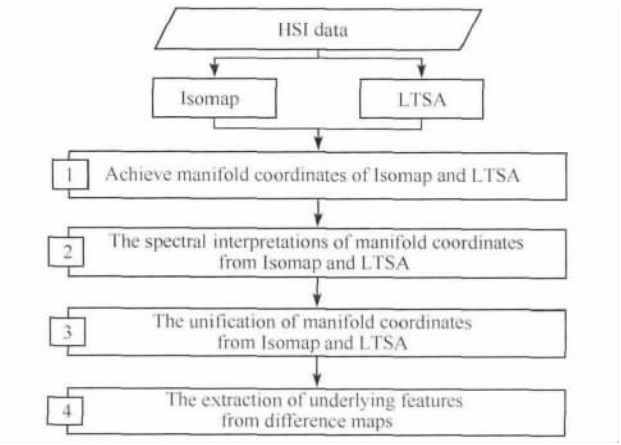

Fig. 1 DMMC method for underlying feature extraction

(1) Manifold coordinates are achieved through Isomap and LTSA with the appropriate parameters. Using the same HSI data integrated with Isomap and LTSA, two manifold coordinates are achieved. The behavior of manifold coordinates depends on the parameter configurations, particularly its intrinsic dimensionality. Owing to the similar manifold structures achieved through different methods, the dimensionality of the embeddings from Isomap and LTSA should be equal. Therefore, only the dimensionality of the Isomap embeddings remains to be estimated, that is, the intrinsic dimensionality of the HSI data. The posterior residual variance method (Tenenbaum, et al., 2000) correlates with the nature of Isomap and has been proven to distinguish manifold structures in a large amount of high-dimensional data accurately, such as handwritten digit and facial images (Tenenbaum, et al., 2000; Yang, 2002). Therefore, in this paper, the posterior residual variance method is employed to estimate the proper intrinsic dimensionality for HSI data.

(2) The spectral interpretations of two coordinates in each dimension are determined. The contrast between manifold coordinates from Isomap and LTSA depends on the correspondences in their spectral interpretations. Otherwise, the differences between these two methods would be rendered meaningless by the lack of theoretical support. Isomap and LTSA have been proven to identify the same manifold structures in facial and handwritten digit images (Lee & Verleysen, 2007), with the same physical interpretations. Similarly, Sun analyzed the spectral interpretations of manifold coordinates by observing and analyzing the changing trends in manifold coordinates and spectral curves. Sun proved that the manifold coordinates in every dimension take spectral features within a certain band interval from the HSI data. The process of spectral interpretation using manifold coordinates is as follows: the distribution maps of manifold coordinates are partitioned into pairs; the distribution map of each pair is divided into cells; spectral vectors of cells are computed along each line or column; and laws regarding spectral interpretations are summarized based on the contrast in changing trends between manifold coordinates and spectral curves within a certain band interval. To validate the conclusions derived from the above process, several groups of pixel points that illustrate the changing trends of manifold coordinates are sampled along the boundary of the distribution maps.

After the above process, both coordinates correspond to each other, thus having the same spectral interpretations. Nevertheless, both coordinates are quite different in scale and may even be reversed when changing directions. Thus, both coordinates are unified in the following step.

(3) Both coordinates are transformed into the uniform system by rescaling coordinates and readjusting the axis directions. Manifold coordinates from Isomap and LTSA are normalized between 0 and 1 using Eq. (1)

$$Ny_{ij} = \frac{y_{ij} - \min(y_{\cdot j})}{\max(y_{\cdot j}) - \min(y_{\cdot j})} \quad i = 1, \cdots, N; j = 1, \cdots, d \tag{1}$$

where Ny_{ij} is the j^{th} normalized coordinate value of pixel point x_i, y_{ij} is the j^{th} original coordinate value of pixel point $\boldsymbol{x}_i$, $\boldsymbol{y}_{\cdot j}$ is the j^{th} coordinate vector; and N and d are the number of points and dimension of the coordinates, respectively.

Moreover, the axis directions of both coordinates are not guaranteed to agree with each other. For example, Table 1 shows that the first coordinates represent spectral features within band 1—56, and the changing direction of the Isomap coordinates coincide with that of the spectral values, in contrast with those of LTSA, which do not coincide with the spectral values. Therefore, readjusting the axis direction is necessary to ensure that the two coordinate systems represent the same spectral features with the same changing directions. The direction readjustment is achieved by comparing the changing trends in the spectral values of both coordinates. Owing to the similarity in spectral interpretations, the shapes of both distribution maps are similar. Consequently, direction adjustment can be completed by comparing both the normalized distribution maps of the manifold coordinates.

(4) The desired underlying features are extracted from the difference maps of manifold coordinates. The differences between two images can usually be quantified using the subtraction operation. Nevertheless, nonlinear manifold features of Isomap and LTSA make the subtraction operation complicated. Therefore, a scale factor α is introduced, and the subtraction relation is given by Eq. (2)

$$\boldsymbol{D}_i = \boldsymbol{N}y_{\text{Isomap}}(i) - \alpha \times \boldsymbol{N}y_{\text{LTSA}}(i) \tag{2}$$

Table 1 Contrast in changing directions between manifold coordinates and DN values in dataset 1

Changing directions of DN values in band intervals	Manifold coordinates			
	Isomap		LTSA	
	First coordinates	Second coordinates	First coordinates	Second coordinates
Band 1—56 (↑)	↑	—	↓	—
Band 57—102 (↑)	—	↑	—	↓
Band 103—191 (↑)	↑	—	↓	—

Note: "↑" means the increasing direction, "—" means the changing direction is unclear, and "↓" means the direction is decreasing.

where $\boldsymbol{D}_i$ stands for the i-th difference map; $\boldsymbol{N}y_{\text{Isomap}}(i)$ and $\boldsymbol{N}y_{\text{LTSA}}(i)$ are the i^{th} coordinates from Isomap and LTSA, respectively; and α is the scale factor, with $0<\alpha\leqslant 1$.

For manifold coordinates in each dimension, the internal difference represents the divergences in spectral features among ground objects within a certain band interval. Therefore, the u nderlying features with spectral values that sharply differ from other ground objects in both manifold maps will appear in the difference map. Finally, using classical image processing methods, the desired underlying features are extracted.

4 EXPERIMENTAL RESULTS AND ANALYSIS

In this section, two sets of HSI data covering different areas will be used to evaluate the proposed method. The memory r equirement of the Isomap algorithm scale is $O(N^3)$, where N is the number of pixels. Therefore, two smaller datasets are extracted from larger datasets to reduce the calculations for the experiments.

4.1 Case study 1

Dataset 1 was taken from the Laboratory for Applications of Remote Sensing at Purdue University. The dataset comprises the HYDICE HSI data for Washington D. C., collected on August 23, 1995, with 210 bands within the 0.4—2.4 μm region of the visible and infrared spectrums. Bands between the 0.9—1.4 μm r egion, where the atmosphere is opaque, have been omitted, leaving 191 bands. The smaller image (Fig. 2) includes the area near the Kutz Bridge with a size of 100 × 100 pixels, containing four primary ground objects: water, road, trees, and grass. In F ig. 3, the spectral curves of most ground objects within band 1—56 are quite crowded and difficult to differentiate. A similar phenomenon can be observed for band 103—191, where most curves are quite similar, except for the lowest water curve. A lthough the differences among all spectral curves are enhanced within band 57—102, spectral curves of grass and road are too similar to separate. After field reconnaissance, the irregular rocks underneath the water are found to have elevated the bed near the river bank compared with the other areas, and the water is divided into the shallow and the deep regions. Spectral signatures in Fig. 3 reflect the subtle heterogeneity underwater. Four groups of spectral curves in the water from different sites are sampled. For band 57—102, the water spectral curves in samples 1, 2, and 3 deviate from the regular spectrum in sample 4, particularly sample 1. With the use of the band near-infrared band 111 and blue band 17, the normal differential water index was utilized to attempt to extract the shallow water. However, the method failed. Therefore, the DMMC method is utilized to extract the shallow water near the river bank.

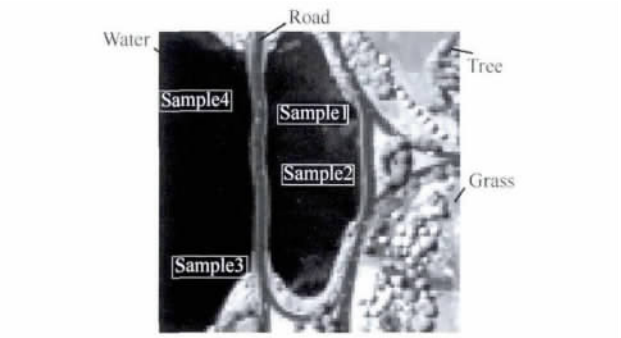

Fig.2 Image of dataset 1

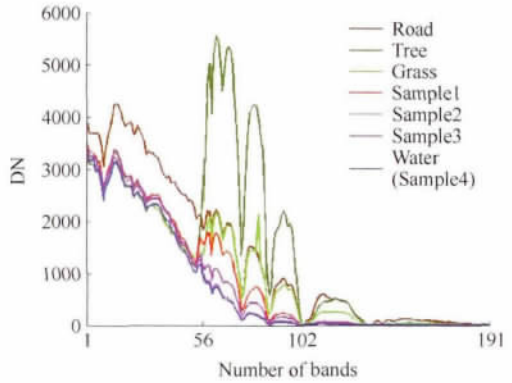

Fig.3 Spectral curves of ground objects in dataset 1

Using the Isomap and LTSA method, two manifold coordinates are obtained. During the process, the neighbor size of I somap and LTSA are 54 and 80, respectively. Using the residual variance method, the proper intrinsic dimension is estimated as 2. With the spectral interpretation method, the changing trends of Isomap and LTSA manifold coordinates and spectral curves are shown in Table 1. From the table, for each method, the first c oordinates denote spectral features in bands 1—56 and 103—191, and the second coordinates represent the spectral features within band 57—102. Therefore, both manifold coordinates have the same spectral interpretations. Nevertheless, the changing d irections of the two coordinates representing the same spectral features are opposite.

The conclusions above are consistent with the distribution of the coordinates from Isomap and LTSA, as shown in Fig. 4 (a) (b), respectively. Both distribution maps are quite similar to each other, with the only difference being the magnitude and the o pposing directions of the shapes. The scales of both coordinates are normalized, and the axis directions are readjusted. In Fig. 4 (c), for both coordinates, most parts coincide with one another, whereas the distribution of the Isomap coordinates is looser than

that of LTSA. This observation affirms the inherent difference between the two methods.

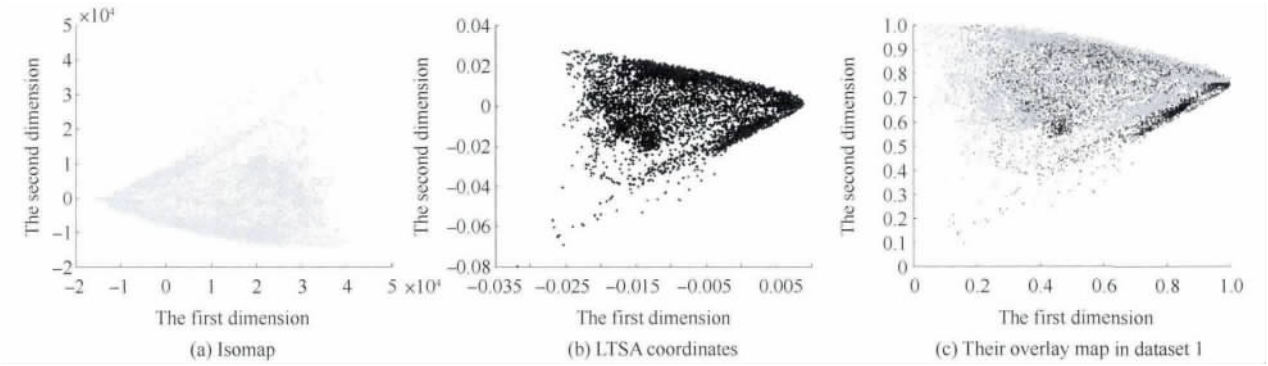

Fig. 4 Distribution of Isomap, LTSA coordinates, and their overlay map in dataset 1

Fig. 5 shows the manifold maps from Isomap and LTSA, as well as the difference maps between them. During the subtraction operation, the scale factor α is 0.87. The shallow water appears in the second difference map, as shown in Fig. 5(f), which is not found in the manifold maps of Isomap and L TSA in Fig. 5(a)—Fig. 5(d). This result is attributed to the significant divergences among the spectral curves of the ground objects within band 57—102, as well as the different capacities of the two coordinates in preserving spectral features. Using the second difference map, the *K*-means and the morphology algorithms are used to segment and extract the shallow water. The extraction result is shown in Fig. 6. The shallow water has been successfully extracted, although the area covered by the bridge was excluded.

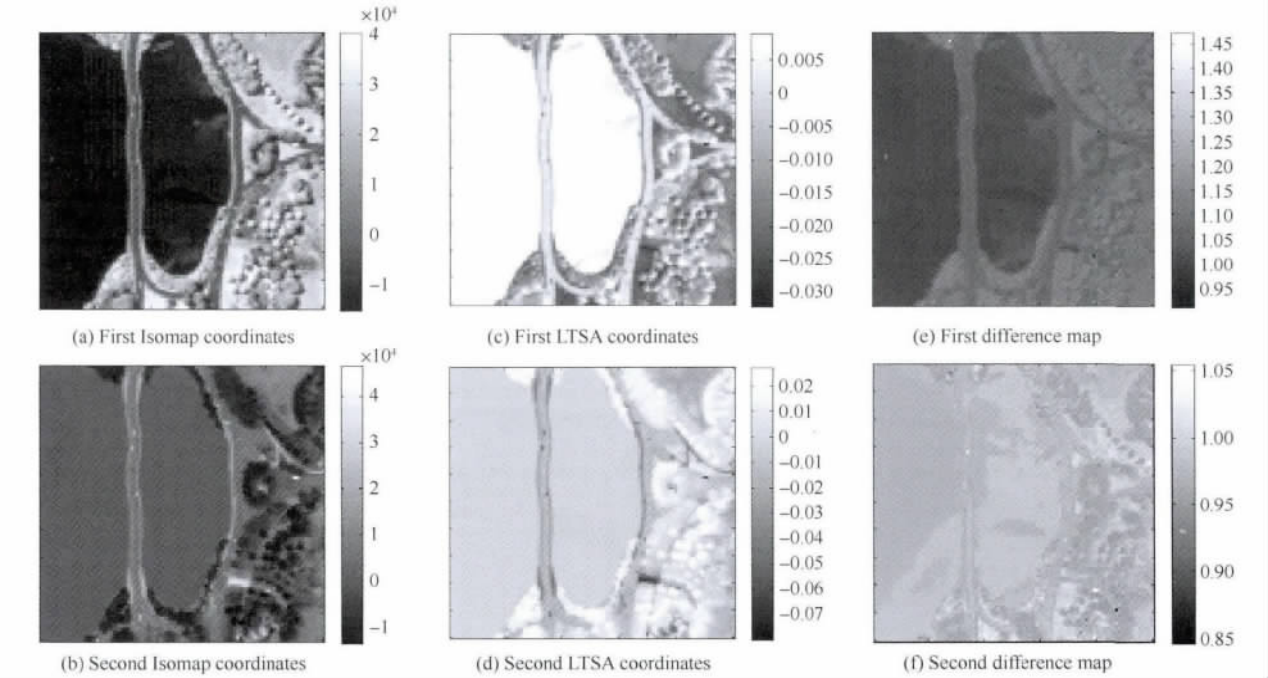

Fig. 5 Manifold maps from Isomap and LTSA and their difference maps in dataset 1

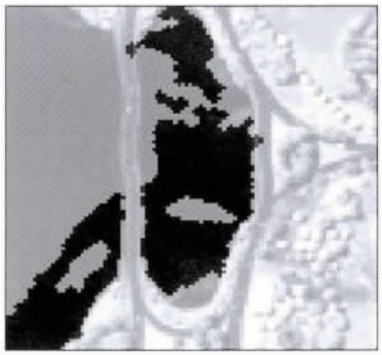

Fig. 6 Extracted shallow water near the river bank

4.2 Case study 2

Taken from the Web site of the Remote Sensing Group in the University of Texas at Austin, dataset 2 comprises the Hyperion HSI data for the Okavango Delta, Botswana. The image was acquired on May 31, 2001, with 30 m spatial resolutions covering the 400—2500 nm portion of the spectrum in 10 nm windows. Isomap and LTSA are both sensitive to noise. Thus, data preprocessing was performed to mitigate the effects of bad detectors, delete low SNR bands, and repair bad lines, leaving the best 40 bands within band 5—44 and covering the spectrum region be-

tween 396 and 796 nm. A smaller dataset with a size of 115 × 115 pixels (Fig. 7(b)) is selected from the larger image (Fig. 7(a)). The small dataset consists of observations from four main identified classes representing the types of swamp land covers. From Fig. 7(b), a narrow road exists in the image scene, which is not evident. The spectral curve of the road in Fig. 8 is globally similar to other ground objects. Comparatively, the divergence between the road and other ground objects within band 1—24 is greater than that within band 25—40. Thus, Hough transform using band 18 was implemented to extract the road. However, this method failed because of the low spatial resolution of the Hyperion data. Therefore, the DMMC method is utilized to extract the road. The neighborhood sizes of Isomap and LTSA are 34 and 280, respectively. After cross-validation, the proper intrinsic dimensionality is 2. Using spectral interpretations, the contrast in the changing directions between the manifold coordinates and DN values is determined, as listed in Table 2. For both methods, the first coordinates denote spectral features within band 1—24, whereas the second coordinates take spectral features within band 25—40. However, the changing directions of both coordinates in the second dimension representing the same spectral features are opposite.

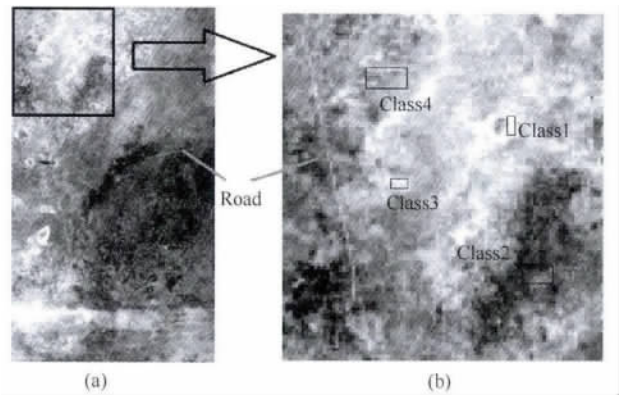

Fig. 7 Image of dataset 2

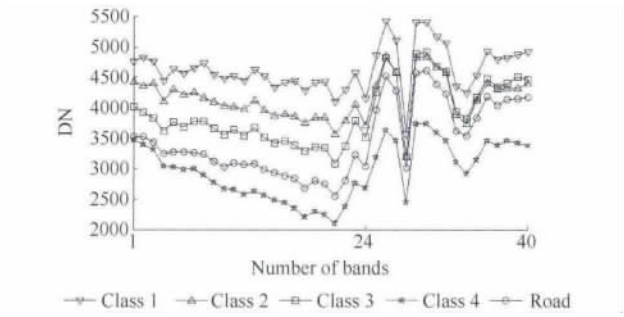

Fig. 8 Spectral curves of ground objects in dataset 2

As shown in Fig. 9(a)(b), the shapes of both maps are similar. These results also show that the axis direction of the second LTSA coordinates is opposite to that of Isomap. Both coordinates are rescaled to [0,1], and the direction of the second LTSA coordinates is readjusted to match that of the Isomap. Fig. 9(c) shows the overlay of the two distribution maps. The scatterings of the two coordinates mostly coincide with one another, whereas the Isomap coordinates scatter more widely than LTSA. This result again validates their intrinsic differences again, as well as the contrast in case study 1.

The manifold and difference maps are shown in Fig. 10. During the subtraction operation, the scale factor α is 0.91. In Fig. 10(c), the road looms in the manifold maps of LTSA rather than that of the Isomap owing to its good performance in preserving local spectral edge features. From the first difference map in Fig. 10(e), the road is more evident than in the original image scene (Fig. 7(b)) and in the manifold maps from Isomap and LTSA (Fig. 10(a)—Fig. 10(d)). Given that both coordinates in the first dimension take spectral features within band 1—24, where the road and other ground objects diverge more significantly from one another and the great divergences between Isomap and LTSA are found when preserving spectral features, the subtle distinctions between the road and other ground objects are amplified and become evident.

Table 2 Contrast in changing directions between manifold coordinates and DN values in dataset 2

Changing directions of DN values in band intervals	Manifold coordinates			
	Isomap		LTSA	
	First coordinates	Second coordinates	First coordinates	Second coordinates
Band 1—24 (↑)	↑	—	↑	—
Band 25—40 (↑)	—	↑	—	↓

Note: "↑" means the increasing direction, "—" means the changing direction is unclear, and "↓" means the direction is decreasing.

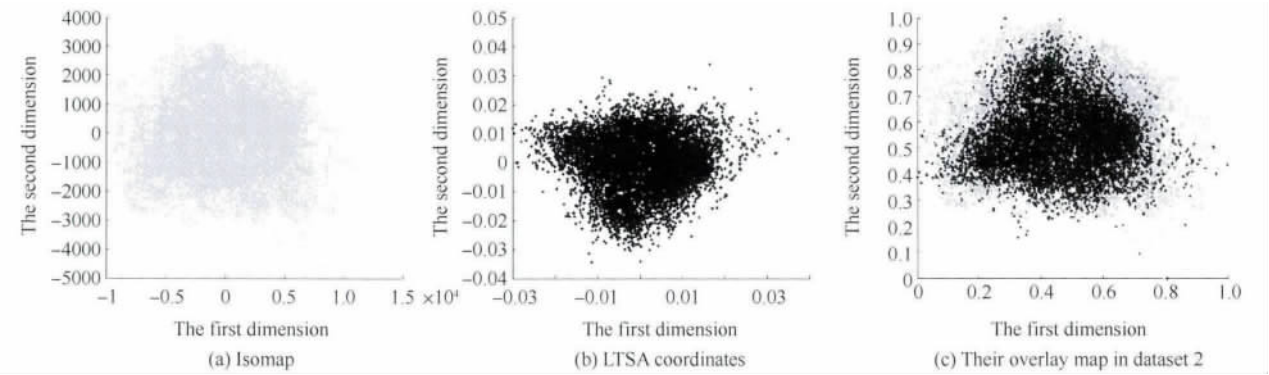

Fig. 9 Distribution of Isomap, LTSA coordinates, and their overlay map in dataset 2

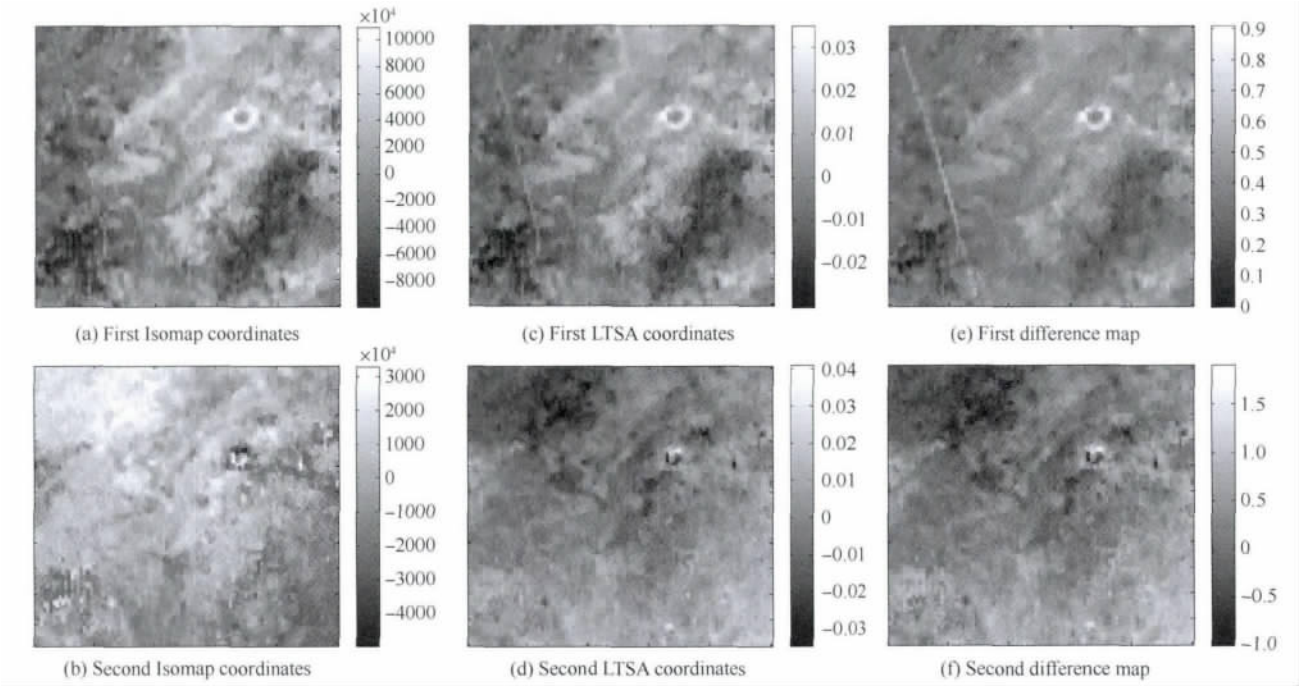

Fig. 10 Manifold maps from Isomap and LTSA and their difference maps in dataset 2

With the first difference map, Hough transform and the morphology algorithms are used to extract the road. The extraction result is shown in Fig. 11.

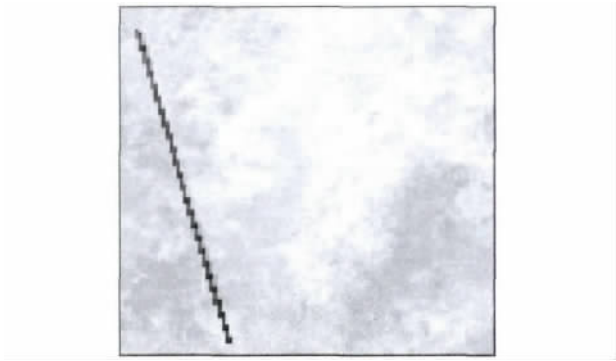

Fig. 11 Extracted road in the large image scene of the swamp

5 CONCLUSIONS AND FUTURE WORK

This paper presents the DMCC method to extract the desired underlying features. First, by observing and comparing the changing trends of manifold coordinates and spectral curves, both manifold coordinates take the same spectral features within a certain band interval from the HSI data. Second, owing to the differences in scale and changing directions, the scales and axis directions of the Isomap and the LTSA coordinates are unified. Finally, with the weighted subtraction operations, the underlying features are extracted using the difference maps of the manifold coordinates. Using two case studies, the proposed method is found to be capable of extracting the underlying features, which cannot be achieved with Isomap and LTSA, such as the shallow water near the river bank and the low-spatial resolution road in the large image scene of the swamp. Meanwhile, both experimental results show that underlying features always appear in the difference map where the spectral curves of the features diverge more significantly from other ground objects. In addition, owing to the diversity of ground objects in HSI data, the ranges of band intervals for the spectral interpretations are quite different in the two case studies. Finally, this paper provides a new method for the extraction of underlying features in HSI data. The DMMC method is helpful in studying the dimensionality reduction of HSI data. However, some problems remain unsolved in the paper. First, owing to the computational complexity of manifold learning, only small datasets were employed to validate our method. Second, considering the difficulty in observing high-dimensional (i. e., more than three) manifold coordinates and spectral curves, two dimensions achieved using residual variances are implemented in the experiments. Finally, the parameter configurations in the DMMC method, such as the neighborhood size k and the scale factor α, are manually determined via cross-validation. These points are suggested directions for future work, and the authors aim to apply the proposed method to the engineering field.

Acknowledgements: The authors would like to thank Professor John. J. Benedetto and Associate Professor Wojciech Czaja of the Norbert Wiener Center for Harmonic Analysis and Applications, Department of Mathematics, University of Maryland, College Park for their helpful suggestions.

REFERENCES

Bachmann C M, Ainsworth T L and Fusina R A. 2005. Exploiting manifold geometry in hyperspectral imagery. IEEE Transactions on Geoscience and Remote Sensing, 43(3): 441 – 454 [DOI: 10.1109/TGRS.2004.842292]

Bachmann C M, Ainworth T L, Fusina R A, Montes M J, Bowles J H, Korwan D R and Gillis D B. 2009. Bathymetric retrieval from hyperspectral imagery using manifold coordinate representations. IEEE

Transactions on Geoscience and Remote Sensing, 47(3): 884 - 897 [DOI: 10.1109/TGRS.2008.2005732]

Belkin M and Niyogi P. 2003. Laplacian eigenmaps for dimensionality reduction and data representation. Neural Computation, 15(6): 1273 - 1396

Chabrillat S, Gotz A F H, Krosley L and Olsen H W. 2002. Use of hyperspectral images in the identification and mapping of expansive clay soils and the role of spatial resolution. Remote Sensing of Environment, 82(2/3): 431 - 445

Chen Y, Crawford M and Ghosh J. 2005. Applying nonlinear manifold learning to hyperspectral data for land cover classification // Proceedings of IEEE International Geoscience and Remote Sensing Symposium. Piscataway: IEEE Press, 6: 4311 - 4314 [DOI: 10.1109/IGARSS.2005.1525872]

Cheng Y B, Ustin S L, Ria O D and Vanderbilt V C. 2008. Water content estimation from hyperspectral images and MODIS indexes in Southeastern Arizona. Remote Sensing of Environment, 112(2): 363 - 374 [DOI: 10.1016/j.rse.2007.01.023]

Crawford M M, Ma L and Kim W. 2011. Exploring nonlinear manifold learning for classification of hyperspectral data. Optical Remote Sensing, (3): 207 - 234

Fong M. 2007. Dimension Reduction on Hyperspectral Images. Los Angeles: UCLA Department of Mathematics

Gillis, D, Bowles J, Lamela G M, Rhea W J, Bachmann C M, Montes M and Ainsworth T. 2005. Manifold learning techniques for the analysis of hyperspectral ocean data // Algorithms and Technologies for Multispectral, Hyperspectral, and Ultraspectral Imagery XI, Proceedings of the Society of Photo-Optical Instrumentation Engineers. SPIE Press: 342 - 351 [DOI: 10.1117/12.603660]

Lee J A and Verleysen M. 2007. Nonlinear Dimensionality Reduction. New York: Springer Verlag

Luo J H, Huang W J, Gu X H, Li N, Ma L, Song X Y, Li W G and Wei C L. 2010. Monitoring stripe rust of winter wheat using PHI based on sensitive bands. Spectroscopy and Spectral Analysis, 30(1): 184 - 187

Ma L, Crawford M M and Tian J. 2010. Anomaly detection for hyperspectral images using local tangent space alignment // Proceedings of IEEE International Geoscience and Remote Sensing Symposium. Piscataway: IEEE Press: 824 - 827

Pu R, Kelly M, Anderson G L and Gong P. 2008. Using CASI hyperspectral imagery to detect mortality and vegetation stress associated with a new hardwood forest disease. Photogrammetric Engineering and Remote Sensing, 74(1): 65 - 75

Roweis S T and Saul L K. 2000. Nonlinear dimensionality reduction by locally linear embedding. Science, 290 (5500): 2323 - 2326 [DOI: 10.1126/science.290.5500.2323]

Sun W W, Liu C, Shi B Q and Li W Y. 2012. Low-dimension manifold feature extraction of hyperspectral imagery using Isomap. Geometrics and Information Science of Wuhan University

Tamayo P, Slonim D, Mesirov J, Zhu Q, Kitareewan S, Dmitrovsky E, Lander E S and Golub T R. 1999. Interpreting patterns of gene e xpression with self-organizing maps: methods and application to hematopoietic differentiation. Proceedings of the National Academy of Sciences of the United States of America, 96(6): 2907 - 2912

Tenenbaum J B, Silva V and Langford J C. 2000. A global geometric framework for nonlinear dimensionality reduction. Science, 290(5500): 2319 - 2323 [DOI: 10.1126/science.290.5500.2319]

Walsh S J, Shao Y, Mena C F and Mccleary A L. 2008. Integration of Hyperion satellite data and a household social survey to characterize the causes and consequences of reforestation patterns in the northern Ecuadorian Amazon. Photogrammetric Engineering and Remote Sensing, 74(6): 725 - 736

Wang X R, Kumar S, Ramos F and Kaupp T. 2006. Probabilistic classification of hyperspectral images by learning nonlinear dimensionality reduction mapping // Proceeding of 9th International Conference on Information Fusion. Piscataway, NJ: IEEE Press: 1 - 8 [DOI: 10.1109/ICIF.2006.301586]

Wang R S, Gan F P, Yan B K, Yang S M and Wang Q H. 2010. Hyperspectral mineral mapping and its application. Remote Sensing for Land and Resources, (1): 1 - 13

Yang H L and Crawford M M. 2011. Manifold alignment for multitemporal hyperspectral image classification // Proceeding of 2011 IEEE International Geoscience and Remote Sensing Symposium (IGARSS). Piscataway, NJ: IEEE Press: 4332 - 4335 [DOI: 10.1109/TGRS.2012.2230445]

Yang M H. 2002. Extended Isomap for pattern classification // Proceedings of Eighteenth National Conference on Artificial Intelligence. Edmonton: AAAI Press: 224 - 229

Zhang Z Y and Zha H Y. 2003. Nonlinear dimension reduction via local tangent space alignment. Intelligent Data Engineering and Automated Learning, 2690: 477 - 481 [DOI: 10.1007/978 - 3 - 540 - 45080 - 1_66]

Zhou Y, Wu B, Li D R and Li R. 2009. Edge detection on hyperspectral imagery via manifold techniques // Proceedings of the First Workshop on Hyperspectral Image and Signal Processing: Evolution in Remote Sensing. Piscataway, NJ: IEEE Press: 1 - 4 [DOI: 10.1109/WHISPERS.2009.5288984]

用流形坐标差异图提取高光谱影像潜在特征

孙伟伟[1]，刘春[1,2]，施蓓琦[1,3]，李巍岳[1]

1. 同济大学 测绘与地理信息学院，上海 200092；
2. 现代工程测量国家测绘地理信息局重点实验室，上海 200092；
3. 上海师范大学 城市信息研究中心，上海 200234

摘　要：等距映射和局部切空间排列降维后，低维流形坐标能够保留原始高光谱影像中地物光谱信息，用于提取原始影像的潜在特征。然而这两种流形方法的理论差异导致其低维坐标继承光谱信息的能力不同，对比这两种流形坐标可凸显出原始影像内部的潜在特征。因此，本文基于等距映射和局部切空间排列非线性降维，提出两种流形坐标的差异图法来提取高光谱影像内部的潜在特征。首先，根据流形坐标的光谱解释确定两种坐标的每一维代表相同的光谱信息。其次，根据相同的光谱特征，归一化两种流形坐标并调整坐标轴方向，统一两种坐标到相同的坐标框架。最后，通过加权流形图相减得到坐标差异图，采用经典的图像处理方法提取潜在特征。采用两个实验并对比等距映射和局部切空间排列方法的降维结果来验证本文方法。结果表明，流形坐标差异图能够成功提取单一流形结果无法得到的潜在特征，如靠河岸的浅水区域和大场景沼泽地中的低分辨率道路。这为高光谱影像的潜在特征提取研究提供了一种新方法。

关键词：高光谱影像，非线性降维，等距映射，局部切空间排列，流形坐标差异图

中图分类号：TP75　　**文献标志码**：A

引用格式：孙伟伟，刘春，施蓓琦，李巍岳. 2013. 用流形坐标差异图提取高光谱影像潜在特征. 遥感学报，17(6)：1327－1443

Sun W W，Liu C，Shi B Q and Li W Y. 2013. Underlying features extraction using difference maps from manifold coordinates of hyperspectral imagery. Journal of Remote Sensing，17(6)：1327－1443 [DOI：10.11834/jrs.20132347]

1　引　言

潜在特征能够反映高光谱影像数据中不明显或非典型的地物光谱信息。例如，海水高光谱影像数据内部蕴含的低维潜在流形特征；高光谱影像中，近河岸水域河床高度不同而由水体内部的细微光谱差异反映出来的深水和浅水区域；描述大范围沼泽地植被的 Hyperion 高光谱影像中，场景内的一条细长道路属于非典型性地物，由于影像空间分辨率较低通常较难提取。潜在特征占地物信息的极小部分，但一直是高光谱影像分析中的热点。潜在特征的提取结果直接关系到后期应用，如地质探测（Chabrillat 等，2002；王润生 等，2010）、环境监测（Cheng 等，2008；Pu 等，2008）和地面侦察（罗菊花 等，2010；Walsh 等，2008）。然而，高光谱影像由于波段众多且相关性强，存在严重“维数灾难”现象，因此常通过降维原始高光谱数据来提取影像内部的潜在特征。

近年来，流形学习降维方法被引入高光谱领域来研究其潜在特征提取。流形学习假设高光谱影像采集于一个低维潜在流形上，通过将原始高光谱数据映射到低维空间实现降维来发掘其潜在特征。目前存在许多流形学习方法，如等距映射 Isomap（Isometric mapping）（Tenenbaum 等，2000）、局部切空间排列 LTSA（Local Tangent Space Alignment）（Zhang 和 Zha，2003）、局部线性嵌入 LLE（Locally Linear Embedding）（Roweis 和 Saul，2000）、拉普拉斯特征映射LE（Laplacian Eigenmaps）（Belkin 和 Niyogi，2003）

收稿日期：2012-12-13；修订日期：2013-03-05；优先数字出版日期：2013-03-12

基金项目：国家重点基础研究发展计划（973 计划）（编号：2013CB733204）；教育部留学回国人员科研启动基金第 37 批资助和现代工程测量国家测绘地理信息局重点实验室开放基金资助项目（编号：TJES1010）

第一作者简介：孙伟伟（1985— ），男，博士研究生，现从事高光谱影像非线性降维、GIS-T 理论及工程应用及压缩感知等研究，已发表论文 16 篇。E-mail：sw8525@gmail.com

及自组织映射 SOM(Self-Organizing Maps)(Tamayo 等,1999)等。其中 Isomap 和 LTSA 分别是流形学习全局和局部方法的代表(Lee 和 Verleysen,2007)。Isomap 能够保持各像元点的测地距离在降维前后保持不变;LTSA 能够保持像元点邻域构成的局部切空间的几何结构在降维前后保持不变。学者针对这两种方法在高光谱影像的潜在特征提取方面已做出一些研究。Isomap 方法方面,Bachmann 等人(2005)引入 Isomap 挖掘低维潜在流形结构用以研究海洋特征。Gills 等人(2005)应用 Isomap 流形学习方法来建模海洋高光谱数据,发现海洋场景能够表达为一组 1 维流形曲线。此后,Bachmann 等人(2009)通过参数化表达非线性 Isomap 流形结构来反映海洋场景的潜在特征。Chen 等人(2005)采用 I somap提取非线性潜在特征并结合基于最短路径的 k-邻域分类器来获取高精度分类结果。Wang 等人(2006)利用 Isomap 发掘训练样本集的潜在流形特征,并基于此训练混合线性模型来实现高精度分类。LTSA 方法方面,Fong(2007)通过实验分析高光谱影像 LTSA 降维的低维流形特征并研究其后续分类性能。Ma 等人(2010)采用 LTSA 降维高光谱影像的少量潜在特征来实现异常探测。Yang 和 Crawford(2011)利用 LTSA 方法提出统一流形排列框架。该方法利用多时态高光谱数据内部统一的潜在流形几何特征来实现多时态分类。Crawford 等人(2011)对比研究 LTSA 和线性降维方法及原始数据的分类性能,发现流形学习发掘的高光谱影像低维潜在特征用于分类效果最好。然而,当前研究仅侧重于单一流形学习提取高光谱影像潜在特征,未考虑过采用两种不同流形学习方法来共同挖掘高光谱影像内部的潜在特征。

经过非线性流形学习降维,高光谱影像的低维流形坐标保留原始影像中各地物的光谱信息,而不同方法的理论差异导致其继承地物光谱信息的能力不同。两种不同流形坐标的对比可以反映其光谱信息继承能力的差异,进而可以将原本在单一流形学习降维结果中的潜在特征凸显出来。两种流形坐标的差异对比需要建立在两种流形嵌入结果的每一维坐标代表相同的光谱信息的基础上。前面工作中(孙伟伟 等,2012),我们提出采用观察对比流形坐标和光谱曲线变化趋势的方法,获得每一维流形坐标的光谱解释。在此基础上,本文从高光谱流形学习降维出发,基于流形坐标的光谱解释提出流形坐标差异图方法来提取影像内部的潜在特征。这为高光谱影像潜在特征提取提供新的研究思路。

2 高光谱影像流形学习降维

流形学习假设高光谱数据均匀采样于统一流形,通过保持某些几何特性将高维数据映射到低维空间而实现非线性降维。在高光谱影像中,Isomap 能够保持高维光谱空间像元点间的测地距离与其对应点在低维空间的欧氏距离基本不变(Tenenbaum 等,2000),LTSA 保持像元点邻域内的局部几何结构不变(Zhang 和 Zha,2003),尤其是图像的光谱边缘特征(Zhou 等,2009)。由于 Isomap 和 LTSA 的显著理论差异,本文采用这两种方法来解释本文方法。然而,本文方法体系也适用于其他流形学习方法。

假设高光谱影像数据为实数向量集 $\boldsymbol{X}=[\boldsymbol{x}_1,\cdots,\boldsymbol{x}_N]^{\mathrm{T}}\in\mathbf{R}^D$,其中 N 和 D 分别为像元点个数和波段数;假设低维流形坐标为向量集 $\boldsymbol{Y}=[\boldsymbol{y}_1,\cdots,\boldsymbol{y}_N]^{\mathrm{T}}\in\mathbf{R}^d$,$d$ 为流形坐标维数;假设每个像元点在光谱空间的邻域为 $\boldsymbol{C}_i=[\boldsymbol{x}_{i_1},\cdots,\boldsymbol{x}_{i_k}]$,其中 k 为邻域大小。

2.1 高光谱影像 Isomap 降维

Isomap 方法通过等距映射高光谱数据到指定的 d 维空间来得到流形坐标(Tenenbaum 等,2000)。首先,通过计算任意像元点 $\boldsymbol{x}_i$ 和 $\boldsymbol{x}_j$ 间欧氏距离来构建邻域。如果 $\boldsymbol{x}_i$ 和 $\boldsymbol{x}_j$ 位于共同的 k-邻域内,则连接两者且边长为两者间的欧氏距离,否则边长为 0。其次,在 k-邻域图的基础上,构建测地距离图。如果 $\boldsymbol{x}_i$ 和 $\boldsymbol{x}_j$ 位于彼此邻域内,两者的测地距离为欧氏距离;否则两者的测地距离通过最短路径采用 Dijkstra 算法来逼近。考虑到最短路径图谱的稳定性,选取图中具有最大连接数的节点,通过多维尺度变换计算得到 d 维流形嵌入。流形坐标 $\boldsymbol{Y}$ 为 $\boldsymbol{\tau}=-\boldsymbol{HSH}/2$ 的前 d 个最大的特征值对应的特征向量,其中 $\boldsymbol{S}$ 为测地距离的平方矩阵,$\boldsymbol{H}$ 为中心矩阵。

2.2 高光谱影像 LTSA 降维

LTSA 方法构建位于每个像元点的局部几何结构,并通过排列彼此重叠的局部切空间来得到全局坐标(Zhang 和 Zha,2003)。首先,类似 Isomap,通过任意像元点 $\boldsymbol{x}_i$ 和 $\boldsymbol{x}_j$ 间的欧氏距离构建邻域。其次,采用 d 维仿射子空间来逼近邻域 $\boldsymbol{C}_i$ 中的像元点,得

到邻域中每一像元点 x_i 的局部坐标 $\Theta_i = Q_i^{\mathrm{T}}(C_i - \bar{x}e_k^{\mathrm{T}})$，式中 Q_i 是 C_i 的中心化矩阵的前 d 个最大的右奇异值所对应的奇异向量，$\bar{x}_i = C_i e^{\mathrm{T}}$ 是 C_i 的中心点。最后，全局坐标 Y 通过局部坐标的仿射变换得到，为排列矩阵 $\Phi = \sum_{i=1}^{N} S_i W_i W_i^{\mathrm{T}} S_i^{\mathrm{T}}$ 的 2 至 $d+1$ 个特征值对应的特征向量，其中 $S_i = [x_{i1}, \cdots, x_{ik}] \in \mathbf{R}^{N\times k}$ 为选择矩阵，$W_i = I - [1_k/\sqrt{k}, V_i][1_k/\sqrt{k}, V_i]^{\mathrm{T}}$，$V_i$ 为中心化矩阵 C_i 的前 d 个最大的左奇异值对应的奇异向量。

3 流形坐标差异图提取潜在特征

流形坐标差异图法利用 Isomap 和 LTSA 降维方法保留原始影像中地物光谱信息的差异来提取潜在特征。流形坐标差异图提取潜在特征的方法如图 1 所示，包括以下步骤：

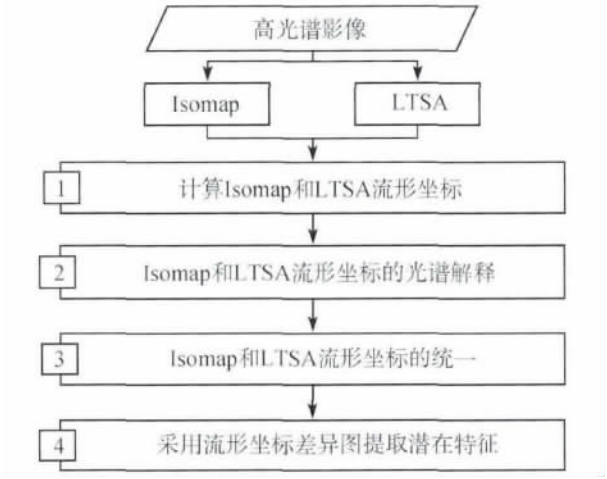

图 1 两种流形坐标差异图的方法流程

(1) 选取合适参数，采用 Isomap 和 LTSA 获取高光谱影像的两种低维流形坐标。流形学习的降维结果依赖于参数选取，尤其是本征维数 d。由于 Isomap和 LTSA 能够同时发掘高维数据的低维流形结构，所以只需估计 Isomap 得到的低维嵌入的维数，即高光谱影像的本征维数。Tenenbaum 提出基于剩余残差的后验式方法与 Isomap 的本质密切相关，而且已经证明能够发现许多高维数据的流形结构，如手写数字图像和人脸图像(Tenenbaum 等，2000；Yang，2002)。因此，本文采用剩余残差法来估计高光谱影像的本征维数 d。

(2) 获取两种坐标每一维的光谱解释并匹配两种流形坐标，确保两种坐标的每一维对应相同的光谱解释。Isomap 和 LTSA 流形坐标的对比依赖于两种流形坐标的每一维所代表的光谱解释一致，否则对比将没有理论基础而失去意义。Isomap 和 LTSA 能够发现人脸图像及手写数字图像中相同的流形结构并具有相同的物理解释(Lee 和 Verleysen，2007)。类似地，我们通过观察对比流形坐标及光谱曲线的变化趋势，得到两种流形坐标各维数的光谱解释，即每一维流形坐标代表一定波段区间内的光谱特征。流形坐标光谱解释的方法如下：将相邻两维流形坐标划为一组；通过设定一定数量且大小一致的矩形窗口来覆盖两维流形坐标分布；观察分析矩形窗口间每一维流形坐标的变化并对比其对应的光谱特征变化趋势，归纳总结出每一维流形坐标对应的光谱特征。同时，在流形坐标分布中随机选取几组采样点，对比分析采样点间流形坐标和光谱特征变化趋势，辅助验证上述观察矩形窗口得到的结论。

Isomap 和 LTSA 的流形坐标尺度及所代表的光谱特征的变化方向并不一致。因此，需要调整两种流形坐标的尺度及坐标轴方向，最终根据每一维坐标代表相同的光谱解释来实现流形坐标的统一。

(3) 通过尺度变换和坐标轴方向调整统一两种坐标到相同坐标系中。采用式(1)将两种流形坐标统一至 0—1：

$$Ny_{ij} = \frac{y_{ij} - \min(y_{\cdot j})}{\max(y_{\cdot j}) - \min(y_{\cdot j})}$$
$$i = 1, \cdots, N; j = 1, \cdots, d \qquad (1)$$

式中，Ny_{ij} 是像元点 x_i 的第 j 个归一化流形坐标值，y_{ij} 是像元点 x_i 的第 j 个原始流形坐标值，$y_{\cdot j}$ 是第 j 维流形坐标向量，N 和 d 是像元点个数和流形坐标维数。

此外，两种坐标的坐标轴方向并不一定相同。例如，表 1 中，Isomap 和 LTSA 流形坐标的第 1 维都代表波段 1—56 间的光谱信息，Isomap 流形坐标的变化方向与光谱值的变化趋势一致，而 LTSA 则相反。因此，需要调整坐标轴的方向，使得两个坐标系统代表相同的光谱解释且变化方向一致。坐标轴方向的调整可通过对比两种流形坐标光谱值的变化趋势得到。此外，两种流形坐标的每一维具有相同光谱解释，流形坐标的分布图非常相似，因此可对比归一化坐标的分布图来实现坐标轴方向调整。

(4) 采用传统图像处理方法从流形坐标差异图提取潜在特征。通常可通过相减操作来获取两幅图像的差异信息。然而 Isomap 和 LTSA 的非线性特性

使得流形图相减操作更加复杂。因此,引入尺度因子 α 进行两种流形坐标间的差异对比,如式(2):

$$\boldsymbol{D}_i = \boldsymbol{N}y_{\text{Isomap}}(i) - \alpha \times \boldsymbol{N}y_{\text{LTSA}}(i) \quad (2)$$

表 1 流形坐标和光谱值的变化方向对比一览表

波段区间 DN 值变化方向	流形坐标			
	Isomap		LTSA	
	第 1 维坐标	第 2 维坐标	第 1 维坐标	第 2 维坐标
波段 1—56(↑)	↑	—	↓	—
波段 57—102(↑)	—	↑	—	↓
波段 103—191(↑)	↑	—	↓	—

注:“↑”代表增大方向,“—”代表变化趋势不明显,“↓”代表减小方向。

式中,$\boldsymbol{D}_i$ 代表第 i 维差异图,$\boldsymbol{N}_{y_{\text{Isomap}}}(i)$ 和 $\boldsymbol{N}_{y_{\text{LTSA}}}(i)$ 是 Isomap 和 LTSA 的第 i 维的归一化流形坐标,α 为尺度因子,$0 < \alpha \leqslant 1$。

高光谱影像的每一维流形坐标中,坐标的内部差异反映其继承对应波段区间的地物间的光谱特征差异。通过加权相减操作,潜在特征凸显于流形坐标差异图中。采用经典图像处理方法,提取得到潜在特征。

4 实验和分析

采用两个实验案例,对比 Isomap 和 LTSA 的降维结果,验证流形坐标差异图法提取潜在特征的可行性。由于 Isomap 算法的内存需求为 $O(N^3)$,其中 N 为像元点个数,因此从两幅较大的影像中选取较小的数据集来减少降维计算量并验证本文方法。

4.1 实验 1

数据 1 来自美国普渡大学应用遥感实验室,为华盛顿区域的 HYDICE 影像。原始影像采集于 1998 年 8 月 23 日,除去由于大气吸收的 900—1 400 nm间的波段,剩余 191 波段,范围为 400—2400 nm,涵盖可见光和近红外区域。选取的小块数据覆盖华盛顿中央广场的 Kutz 桥区域(图 2),大小为 100 × 100 像元,包含水体、道路、树木和草地 4 类主要地物。图 3 看出,波段为 1—56 时,大多数地物光谱曲线非常接近,难以区分。类似现象在波段为 103—191 时,大多数光谱曲线非常相似,除水体光谱 DN 值最低。在波段 57—102,地物间光谱区分能力增强,但道路与草地的光谱特征较为接近,仍较难区分。实地踏勘发现,河岸水下不规则石块导致靠岸的河床比其他区域高,水位较浅,整个水域可大致分为浅水和深水区域。浅水区域的河床内部高度并不一致,可以从 4 个采样区得到的水体光谱曲线反映出来(图 3)。在波段 57—102,样本 1、样本 2 和样本 3 的光谱曲线偏离标准光谱(样本 4),但各样本间光谱差异较小,较难区分。选用原始影像中近红外 111 波段和蓝光 17 波段,采用经典的水体归一化指数(NDWI),无法从水体中提取浅水区域。因此,采用流形坐标差异图法提取近岸浅水区域。

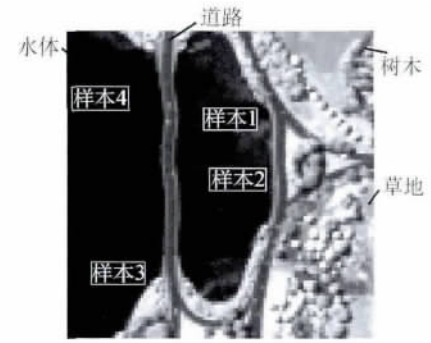

图 2 数据 1

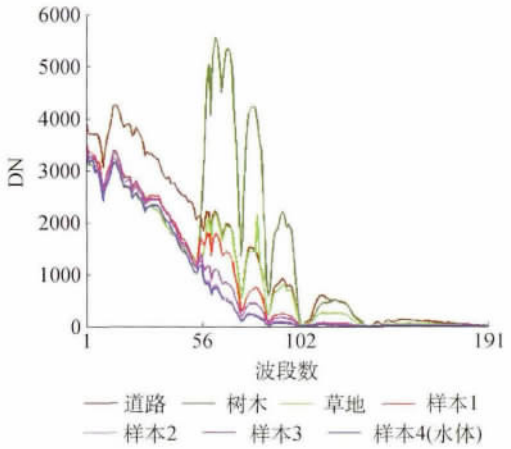

图 3 数据 1 中主要地物的光谱曲线

经过交叉验证，Isomap 和 LTSA 降维中邻域大小分别为 54 和 80；采用剩余残差法得到本征维数为 2。采用流形坐标的光谱解释方法，对比观察光谱曲线及两种流形坐标，Isomap 和 LTSA 流形坐标与波段区间的光谱值的变化趋势如表 1 所示。总结发现，对于 Isomap 和 LTSA 两种降维方法，第 1 维坐标代表波段 1—56 及波段 103—191 的光谱特征；第 2 维坐标代表波段 57—102 的光谱特征。同时可以看出，具有相同光谱解释的 Isomap 和 LTSA 两种坐标的变化趋势相反。

同时，图 4(a)(b)中 Isomap 和 LTSA 坐标分布可以看出，两者的坐标分布非常相似，除了尺度和形状朝向上的差异。归一化两种坐标至 0—1，两种流形坐标分布的叠加如图 4(c)所示。图中两种坐标分布大部分重合，而 Isomap 坐标分布比 LTSA 更加稀疏，这验证了两种方法的理论差异。

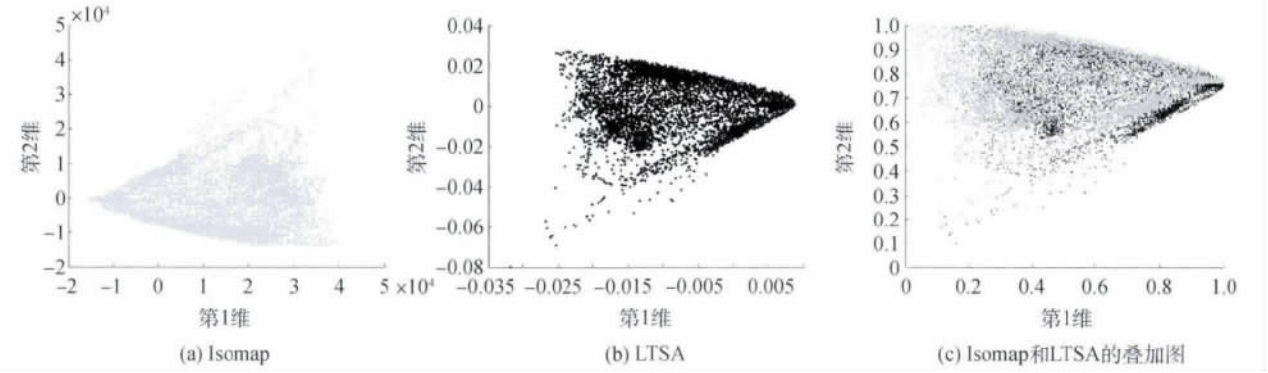

图 4 Isomap 和 LTSA 的坐标分布及两者的叠加图

图 5 为 Isomap 和 LTSA 的流形图及两者的差异图，其中尺度因子 α 设置为 0.87。图 5(f)可以看出，浅水区域出现于第 2 维差异图中，并未出现于 Isomap 和 LTSA 的流形图中(图 5(a)—(d))。这是由于波段 57—102 间各地物的光谱差异相对较大，以及 Isomap 和 LTSA 方法在保持地物光谱特征方面的差异，使得浅水区域通过加权流形坐标相减而变得清晰。利用第 2 维差异图，采用 K-均值聚类和腐蚀膨胀形态学算法，得到最终的浅水区域提取结果，如图 6 所示。可以看出，除被 Kutz 桥掩盖的水体，浅水区域被基本提取。

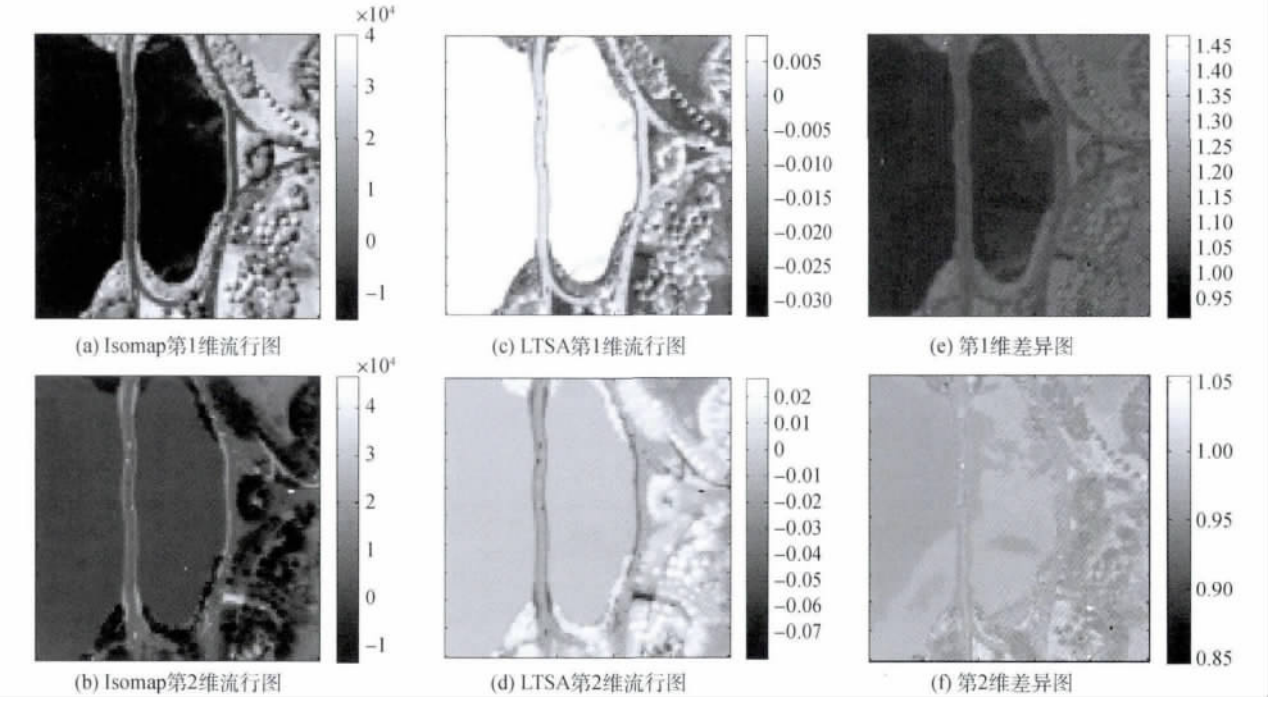

图 5 数据 1 中 Isomap 和 LTSA 的流形图及两者的差异图

图6 靠河岸的浅水区域的提取结果

4.2 实验2

数据2来自美国德克萨斯大学奥斯丁分校遥感组,为博茨瓦纳的奥卡万戈三角洲区域的Hyperion高光谱数据。数据采集于2001年5月31日,空间分辨率为30 m,光谱分辨率为10 nm,光谱范围是400—2500 nm。Isomap和LTSA方法对噪声非常敏感,因此通过前期数据处理,删除低信噪比波段并修复坏线,剩余40波段,波段区间为[5—44],波长范围为396—796 nm。从图7(a)的大幅影像中选取较小区域,大小为115×115像元,如图7(b)所示。小幅图像为奥卡万戈三角洲沼泽地区域,主要地物类别为4类沼泽地植被,光谱曲线如图8所示。图7(b)中,大范围沼泽地中隐现一条细长道路,属于非典型地物。相比而言,在波段1—24,道路与其他地物的光谱差异比在波段25—40明显。利用18波段并结合霍夫变换来提取该道路,但由于空间分辨率较低,道路像元的光谱特征和主要地物非常相似,较难提取得到。因此,采用流形坐标差异法提取沼泽地中的低分辨率道路。

降维过程中,通过交叉验证,Isomap和LTSA的邻域大小分别为34和280,剩余残差法得到本征维数为2。采用流形学习光谱解释方法,对比观察两种流形坐标与光谱值的变化趋势如表2所示。总结得出以下结论:Isomap和LTSA坐标的第1维都代表波段1—24的光谱信息;第2维坐标代表波段25—40的光谱信息,然而两种方法的第2维坐标所代表的光谱信息变化趋势相反。

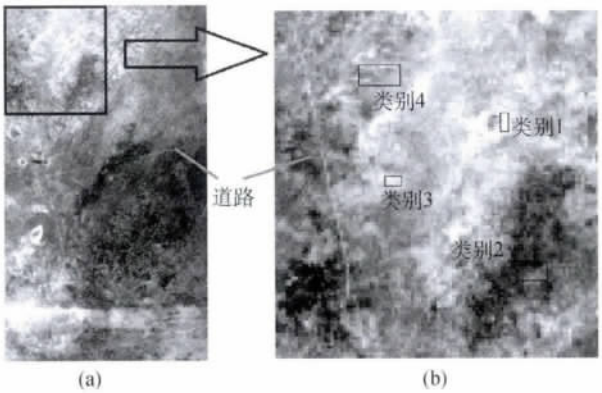

图7 数据2

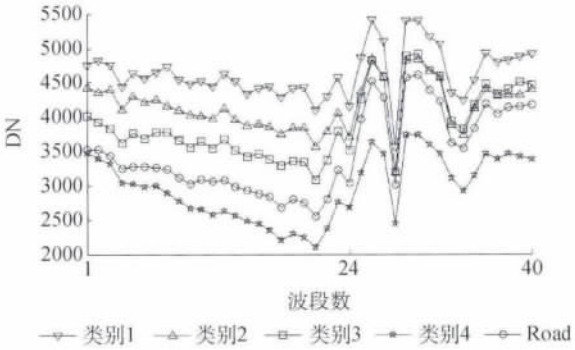

图8 数据2中主要地物光谱曲线

表2 流形坐标和光谱值的变化方向对比一览表

波段区间DN值变化方向	流形坐标			
	Isomap		LTSA	
	第1维坐标	第2维坐标	第1维坐标	第2维坐标
波段1—24(↑)	↑	—	↑	—
波段25—40(↑)	—	↑	—	↓

注:“↑”代表增大方向,“—”代表变化趋势不明显,“↓”代表减小方向。

图9(a)(b)中两种坐标的分布看出,Isomap和LTSA流形坐标分布图非常相似,仅存在垂直向上的差异。这同样说明LTSA的第2维坐标的坐标轴方向与Isomap相反。两种坐标都被归一化至0—1,同时调整LTSA的第2维坐标轴方向与Isomap对应坐标一致。图9(c)为调整后的两种坐标分布图的叠

加，可看出两者坐标大部分非常吻合，而 Isomap 坐标比 LTSA 分布更广泛。这再次验证两种方法的差别，并支持实验 1 中的对比结论。

图 10 为 Isomap 和 LTSA 方法的流形图及其差异图，其中尺度因子 α 为 0.91。可以看出，由于 LTSA 在局部光谱边缘特征方面的优势，道路隐现于 LTSA 的第 1 维流形图（图 10（c））。同时，图 10（e）的第 1 维差异图看出，道路轮廓比原始影像（图 7（b））及 Isomap 和 LTSA 的流形图（图 10（a）—（d））中更加清晰。这是由于第 1 维流形坐标保留波段 1—24 的光谱信息，而 1—24 波段内，道路与主要地物区分较强，再加上两种方法保持地物光谱信息的差异，最终使得道路通过加权流形图相减而变得更加明显。利用第 1 维流形图，采用霍夫变换及形态学算法来提取道路，结果如图 11。

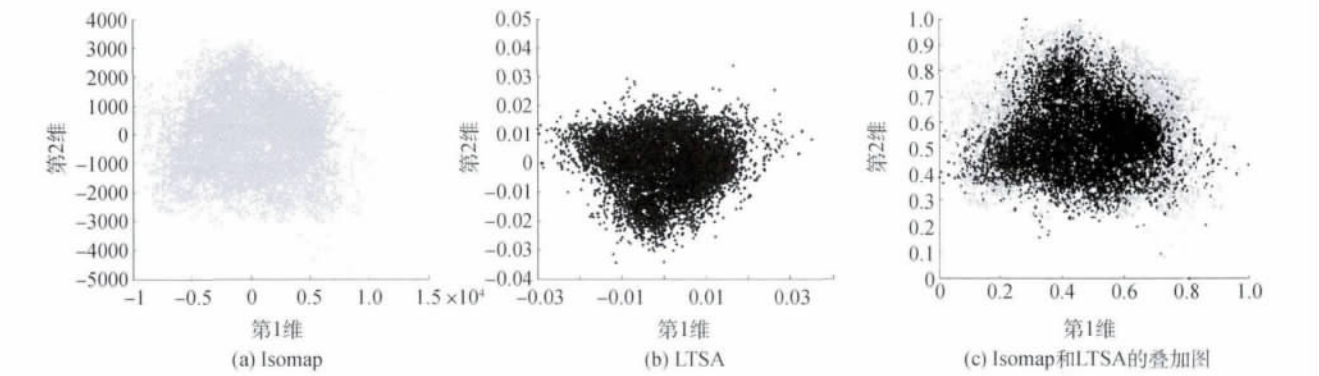

图 9 Isomap 和 LTSA 的坐标分布及两者的叠加图

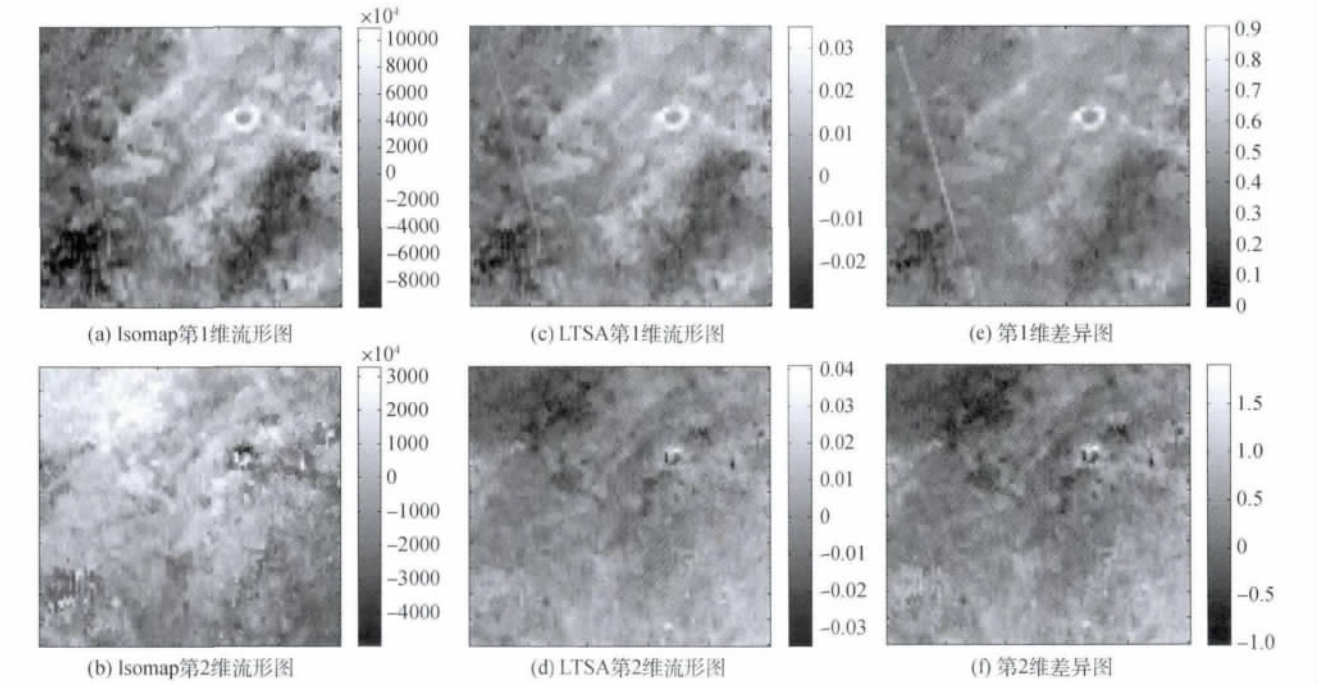

图 10 数据 2 中 Isomap 和 LTSA 的流形图及两者的差异图

5 结论和展望

本文提出流形坐标差异图法，利用这两种流形坐标代表的光谱信息差异来提取影像内部的潜在特征。首先，通过观察对比流形坐标和光谱曲线特征，找到每一维流形坐标所对应的光谱解释。同时，Isomap 和 LTSA 流形坐标的尺度差别较大且变化方向不一致，所以统一两种坐标尺度及坐标轴方向。最后，通过两种流形图的加权相减，利用流形差异图提取潜在特征。基于两个应用实例，实验结果证明本文提出的方法能够提取 Isomap 和 LTSA 无法得到的

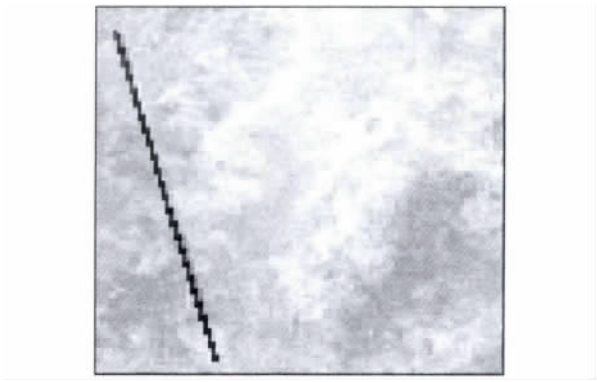

图 11 大场景沼泽地中低分辨率道路的提取结果

潜在特征,如靠岸的浅水区域和大场景沼泽地中的低分辨率道路。实验结果同时表明,潜在特征通常出现于该地物光谱特征与其他地物差异较大的流形差异图中。此外,实验中光谱解释所对应的波段区别差别很大及对应流形坐标的维数不同,这是由不同影像数据和影像中地物分布不规则和类别多样性造成的。本文研究为提取高光谱影像潜在特征提供一种新的研究方法,为高光谱影像的流形学习降维研究提供参考和借鉴,但仍存在一些问题和不足。首先,由于流形学习算法计算复杂度高,本文仅采用较小的数据来验证方法。其次,考虑到观察对比高维(3 维及以上)流形坐标与光谱曲线的实践难度,文中仅采用剩余残差法选择 2 维的流形坐标来展开实例研究。最后,流形坐标差异图方法中参数的选取,如 Isomap 和 LTSA 方法中邻域 k 及差异图中尺度因子 α,都是通过交叉验证来人工选取,还未实现自动化或半自动化智能估计。这些都是接下来重点研究的方向。

志 谢 感谢美国马里兰大学帕克分校数学系诺伯特维纳中心的 John. J. Benedetto 教授和 Wojciech Czaja 副教授对论文的指导和帮助。

参考文献(References)

Bachmann C M, Ainsworth T L and Fusina R A. 2005. Exploiting manifold geometry in hyperspectral imagery. IEEE Transactions on Geoscience and Remote Sensing, 43(3): 441 – 454 [DOI: 10.1109/TGRS.2004.842292]

Bachmann C M, Ainworth T L, Fusina R A, Montes M J, Bowles J H, Korwan D R and Gillis D B. 2009. Bathymetric retrieval from hyperspectral imagery using manifold coordinate representations. IEEE Transactions on Geoscience and Remote Sensing, 47(3): 884 – 897 [DOI: 10.1109/TGRS.2008.2005732]

Belkin M and Niyogi P. 2003. Laplacian eigenmaps for dimensionality reduction and data representation. Neural Computation, 15(6): 1273 – 1396

Chabrillat S, Gotz A F H, Krosley L and Olsen H W. 2002. Use of hyperspectral images in the identification and mapping of expansive clay soils and the role of spatial resolution. Remote Sensing of Environment, 82(2/3): 431 – 445

Chen Y, Crawford M and Ghosh J. 2005. Applying nonlinear manifold learning to hyperspectral data for land cover classification // Proceedings of IEEE International Geoscience and Remote Sensing Symposium. Piscataway: IEEE Press, 6: 4311 – 4314 [DOI: 10.1109/IGARSS.2005.1525872]

Cheng Y B, Ustin S L, Ria O D and Vanderbilt V C. 2008. Water content estimation from hyperspectral images and MODIS indexes in Southeastern Arizona. Remote Sensing of Environment, 112(2): 363 – 374 [DOI: 10.1016/j.rse.2007.01.023]

Crawford M M, Ma L and Kim W. 2011. Exploring nonlinear manifold learning for classification of hyperspectral data. Optical Remote Sensing, (3): 207 – 234

Fong M. 2007. Dimension Reduction on Hyperspectral Images. Los Angeles: UCLA Department of Mathematics

Gillis, D, Bowles J, Lamela G M, Rhea W J, Bachmann C M, Montes M and Ainsworth T. 2005. Manifold learning techniques for the analysis of hyperspectral ocean data // Algorithms and Technologies for Multispectral, Hyperspectral, and Ultraspectral Imagery XI, Proceedings of the Society of Photo-Optical Instrumentation Engineers. SPIE Press: 342 – 351 [DOI: 10.1117/12.603660]

Lee J A and Verleysen M. 2007. Nonlinear Dimensionality Reduction. New York: Springer Verlag

罗菊花, 黄文江, 顾晓鹤, 李宁, 马丽, 宋晓宇, 李伟国, 韦朝领. 2010. 基于 PHI 影像敏感波段组合的冬小麦条锈病遥感监测研究. 光谱学与光谱分析, 30(1): 184 – 187

Ma L, Crawford M M and Tian J. 2010. Anomaly detection for hyperspectral images using local tangent space alignment // Proceedings of IEEE International Geoscience and Remote Sensing Symposium. Piscataway: IEEE Press: 824 – 827

Pu R, Kelly M, Anderson G L and Gong P. 2008. Using CASI hyperspectral imagery to detect mortality and vegetation stress associated with a new hardwood forest disease. Photogrammetric Engineering and Remote Sensing, 74(1): 65 – 75

Roweis S T and Saul L K. 2000. Nonlinear dimensionality reduction by locally linear embedding. Science, 290 (5500): 2323 – 2326 [DOI: 10.1126/science.290.5500.2323]

孙伟伟, 刘春, 施蓓琦, 李巍岳. 2012. 等距映射用于高光谱影像低维流形特征提取. 武汉大学学报(信息科学版)

Tamayo P, Slonim D, Mesirov J, Zhu Q, Kitareewan S, Dmitrovsky E, Lander E S and Golub T R. 1999. Interpreting patterns of gene expression with self-organizing maps: methods and application to hematopoietic differentiation. Proceedings of the National Academy of Sciences of the United States of America, 96(6): 2907 – 2912

Tenenbaum J B，Silva V and Langford J C. 2000. A global geometric framework for nonlinear dimensionality reduction. Science，290(5500)：2319－2323 [DOI：10.1126/science.290.5500.2319]

Walsh S J，Shao Y，Mena C F and Mccleary A L. 2008. Integration of Hyperion satellite data and a household social survey to characterize the causes and consequences of reforestation patterns in the northern Ecuadorian Amazon. Photogrammetric Engineering and Remote Sensing，74(6)：725－736

Wang X R，Kumar S，Ramos F and Kaupp T. 2006. Probabilistic classification of hyperspectral images by learning nonlinear dimensionality reduction mapping // Proceeding of 9th International Conference on Information Fusion. Piscataway，NJ：IEEE Press：1－8 [DOI：10.1109/ICIF.2006.301586]

王润生，甘甫平，闫柏琨，杨苏明，王青华. 2010. **高光谱矿物填图技术与应用研究**. **国土资源遥感**，(1)：1－13

Yang H L and Crawford M M. 2011. Manifold alignment for multitemporal hyperspectral image classification // Proceeding of 2011 IEEE International Geoscience and Remote Sensing Symposium (IGARSS). Piscataway，NJ：IEEE Press：4332－4335 [DOI：10.1109/TGRS.2012.2230445]

Yang M H. 2002. Extended Isomap for pattern classification // Proceedings of Eighteenth National Conference on Artificial Intelligence. Edmonton：AAAI Press：224－229

Zhang Z Y and Zha H Y. 2003. Nonlinear dimension reduction via local tangent space alignment. Intelligent Data Engineering and Automated Learning，2690：477－481 [DOI：10.1007/978－3－540－45080－1_66]

Zhou Y，Wu B，Li D R and Li R. 2009. Edge detection on hyperspectral imagery via manifold techniques // Proceedings of the First Workshop on Hyperspectral Image and Signal Processing：Evolution in Remote Sensing. Piscataway，NJ：IEEE Press：1－4 [DOI：10.1109/WHISPERS.2009.5288984]